

Comparative Analysis of the Mechanisms of Fast Light Particle Formation in Nucleus-Nucleus Collisions at Low and Intermediate Energies

A.S. DENIKIN^{*)} and V.I. ZAGREBAEV

Joint Institute for Nuclear Research, Dubna, 141980 Russia

(Received February 5, 2001; in final form, May 25, 2001)

The dynamics and the mechanisms of preequilibrium-light-particle formation in nucleus-nucleus collisions at low and intermediate energies are studied on the basis of a classical four-body model. The angular and energy distributions of light particles from such processes are calculated. It is found that, at energies below 50 MeV per nucleon, the hardest section of the energy spectrum is formed owing to the acceleration of light particles from the target by the mean field of the projectile nucleus. Good agreement with available experimental data is obtained.

§1. INTRODUCTION

The formation of preequilibrium light particles (n , p , d , t , α) in nucleus-nucleus collisions is determined by the evolution that the nuclear system involved in the reaction being considered undergoes at the initial reaction stage. It is well known that the cross section for light-particle yield from heavy-ion collisions constitutes a significant part of the total reaction cross section even at low energies of about 10 MeV per nucleon; that is, the formation of light particles is peculiar to all nuclear reactions featuring heavy ions. This implies that investigation of the mechanism of formation of such particles may furnish direct information both about the dynamics of the initial stage of the reaction and about the potential and dissipative forces of nucleus-nucleus interaction. Basic regularities in the behavior of the angular and energy distributions of light particles - in particular, the presence of high-energy components in them - cannot be described within the usual statistical model of excited-nucleus decay¹⁾⁻¹⁶⁾. A large number of theoretical approaches considering various mechanisms of fast-light-particle formation have been proposed in recent years. These include the moving-source model³⁾, the hot-spot model¹⁷⁾, the model of disintegration and incomplete fusion¹⁸⁾⁻²¹⁾, the model of dissipative disintegration accompanied by the massive-transfer process^{22), 23)}, and the Fermi-jet model and models close to it in spirit²⁴⁾⁻²⁹⁾. A detailed survey of experimental and theoretical studies devoted to this problem can be found in³⁰⁾. In view of a considerable improvement of the technical characteristics of measuring equipment, it became possible to measure precisely the angular and energy spectra of light particles. The most recent experiments discovered preequilibrium light particles whose velocities are more than twice as great as the velocity of beam particles¹¹⁾⁻¹⁴⁾. This sparked

^{*)} E-mail: denikin@jinr.ru

anew the interest of researchers in the problem and reinforced motivations behind the hypothesis that nucleon-nucleon collisions play a dominant role in the formation of ultrafast light particles. In the present study, the role of nucleon-nucleon collisions and of mean nuclear fields in the formation of the spectra of preequilibrium light particles is investigated in detail on the basis of the four-dimensional classical model of nucleus-nucleus collisions. Among other things, it is shown that the effect of mean nuclear fields is crucial at beam energies in the region $E_0 < 50$ MeV per nucleon. The ensuing exposition is organized as follows. In Section 2, we give an account of the model that underlies the present analysis of the methods used here to calculate the differential cross sections for light particles formed in nucleus-nucleus collisions and the multiplicities of these particles. In Section 3, we consider various mechanisms of preequilibrium-light-particle formation that are realized in the model developed here. In Section 4, the results of our calculations for the above cross sections are compared with experimental data. In Section 5, we investigate the dependence of our results on physical model parameters, such as potentials of fragment interaction and forces of nuclear friction. In the last section, we formulate basic conclusions that can be drawn from our study.

§2. FOUR-BODY MODEL OF NUCLEUS-NUCLEUS COLLISIONS

In studying the mechanisms of light-particle formation in nucleus-nucleus collisions, we rely here on a semi-classical four-body model that makes it possible to establish explicitly the role of mean nuclear fields and the role of nucleon-nucleon collisions. Within this model, the projectile (P) and the target (T) nucleus are taken in the form of two-particle subsystems; that is, $P = (A + a)$ and $T = (B + b)$, where A and B stand for heavy nuclear cores, while a and b represent light fragments (n, p, d, t, α). Introducing six pair interaction potentials $V(r_{ij})$ (where the subscripts i and j correspond to particles A, B, a , and b and where $\vec{r}_{ij} = (\vec{r}_i - \vec{r}_j)$ is the distance between particles i and j), we specify the Hamiltonian for the system being considered as

$$H = \sum_i \frac{\vec{p}_i^2}{2m_i} + \sum_{ij, i \neq j} V(r_{ij}). \quad (2.1)$$

The potentials taken to represent the heavy-core interaction with light particles are chosen here in the Woods-Saxon form with the parameters corresponding to optical potentials constructed on the basis of an analysis of elastic-scattering data³¹⁾. The interaction between cores A and B is chosen in the form of the Coulomb potential energy and the nuclear interaction simulated by either the proximity potential from³²⁾ or the Woods-Saxon potential. Coupling to reaction channels that are not taken explicitly into account within the four-body model was described in terms of dissipative forces introduced with the aid of the corresponding dissipative function D . In order to solve numerically the set of equations of motion

$$\frac{d\vec{r}_i}{dt} = \frac{\partial H}{\partial \vec{p}_i}; \quad \frac{d\vec{p}_i}{dt} = -\frac{\partial H}{\partial \vec{r}_i} - \frac{\partial D}{\partial \vec{v}_i} \quad (2.2)$$

where p_i and v_j are the vectors of, respectively, the momentum and the velocity of particle i , it is necessary to preset boundary conditions for the vectors \vec{r}_i and \vec{p}_i . The internal spatial configuration of the projectile nucleus is completely determined by the vector \vec{r}_{Aa} of the relative distance between the projectile fragments, the energy E_{Aa} of their relative motion (that is, the projectile binding energy), and the vector \vec{l}_{Aa} of the orbital angular momentum associated with the relative motion of these particles. The components of the vector $\vec{r}_{Aa}(t=0)$ are chosen via their generation at random on the basis of some spatial-distribution function. Our calculations revealed that the form of the radial dependence of this distribution affects only slightly the final result. This is explained by the specificity of the classical model, where, as the time of approach of the nuclei involved increases, any initial distribution tends to a purely classical distribution, in which case the particle resides for a longer time in the vicinity of the external turning point. At the same time, a decrease in the time of approach entails an increase in the computational error. In the case being considered, the relative position of particles A and a was chosen to be equiprobable in the energetically allowed region of space. In order to determine the relative momentum \vec{p}_{Aa} unambiguously, it is necessary to fix, in addition to the relative energy E_{Aa} , the distance $|\vec{r}_{Aa}|$ between the fragments, and the orbital angular momentum $|\vec{l}_{Aa}|$, one of the components of the vector \vec{l}_{Aa} as well (this is also done via a generation at random). Applying the same procedure to the target nucleus and specifying the relative motion of the centers of mass of the target and the projectile nucleus in accordance with a given reaction, we fully define boundary conditions that are necessary for solving the set of Eqs. (2.2). The function D in Eqs. (2.2) is an ordinary Rayleigh dissipative function that describes the dissipation of energy and of the angular momentum of the relative motion of the nuclei involved. In the case where fragments a and b are much lighter than cores A and B , it is assumed that the friction forces act only between the cores. In terms of spherical coordinates, the Rayleigh function then has the diagonal form

$$D = \frac{1}{2}f(r) \left(\gamma_r \dot{r}^2 + \gamma_\theta r^2 \dot{\theta}^2 + \gamma_\phi r^2 \sin^2 \theta \dot{\phi}^2 \right), \quad (2.3)$$

$$\gamma_\theta = \gamma_\phi = \gamma_t,$$

where γ_r and γ_t are, respectively, the radial and the tangential coefficient of friction; $f(r)$ is the radial form factor for dissipative forces; and $\vec{r} = \vec{r}_A - \vec{r}_B = \{r, \theta, \phi\}$ is the vector of the relative motion of particles A and B . In choosing the coefficients γ_r and γ_t and the form factor $f(r)$, we followed³³. Thus, we have a set of 24 coupled classical differential equations of motion [set of Eqs. (2.2)]; we construct here its numerical solutions directly in the laboratory frame using Cartesian coordinates. By performing a numerical integration of Eqs. (2.2) with respect to time for different initial conditions, we arrive at various output channels. It can easily be shown that, within the four-body model used, there are 15 output reaction channels. These are scattering channels, channels involving the breakup of the projectile or the target (or

both), particle-transfer channels, and channels of complete and incomplete fusion:

$$P + T \equiv (Aa) + (Bb) \rightarrow \begin{cases} (Aa) + (Bb), \\ A + a + B + b, \\ \dots, \\ (Ab) + (Ba), \\ (Aab) + B, \\ \dots, \\ (ABb) + a, \\ (ABab). \end{cases} \quad (2.4)$$

Here, parentheses enclose bound states of two or more fragments. In describing the relative motion of particles $(a + B)$ and $(b + A)$, the differential cross sections for various channels can be estimated more correctly in terms of the probability of their absorption. We define this probability P_{ij}^{abs} as

$$\begin{aligned} P_{ij}^{abs} &= 1 - \exp\left(-\frac{s_{ij}}{\lambda_{ij}}\right) \\ &= 1 - \exp\left(-\int_{tr} \frac{2W_{ij}(r')dr'}{\hbar v_{ij}(r')}\right), \end{aligned} \quad (2.5)$$

where s_{ij} is the distance that particle i travels in nucleus j , λ_{ij} is the corresponding mean range, $W_{ij}(r)$ is the imaginary part of the optical potential (it describes absorption in the case of the elastic scattering of particle i by nucleus j), and v_{ij} is their relative velocity. Integration in (2.5) is performed along the actual trajectory of the fragments.

In classical dynamics, the relative energy of two particles in a bound state can take any admissible value – in particular, collapse onto the potential-well bottom is possible. In studying the formation of bound states of two or more particles in output channels, it is therefore necessary to check additionally their relative energy in order to eliminate unphysical events where the energy of the fragments is below the experimental energy of their bound state.

For any reaction channel in (2.4), the differential cross section is calculated by the formula

$$\begin{aligned} \frac{d^2\sigma_\mu}{dEd\Omega}(E, \theta) &= \int_0^\infty 2\pi\rho \\ &\times \left[\frac{\Delta N_\mu(\rho, E, \theta)}{N_{tot}(\rho)} \frac{1 - P_\mu(\rho)}{2\pi \sin\theta \Delta\theta \Delta E} \right] d\rho, \end{aligned} \quad (2.6)$$

where $\Delta N_\mu(\rho, E, \theta)$ is the number of events in which the system goes over into the channel μ , at a given value of the impact parameter ρ , $N_{tot}(\rho)$ is the total number of simulated events for a given value of ρ , and $P_\mu(\rho)$ is the probability of absorption in this channel. The bracketed factor in the integrand on the right-hand side of (2.6) is the partial differential multiplicity for the event type being considered. Upon

individually integrating this factor with respect to the impact parameter, we would obtain the differential multiplicity, which is a quantity often measured in experiments instead of the corresponding cross section.

The main contribution to the soft section of the energy spectrum of light particles comes from the evaporation of particles from excited reaction products. As a rule, the multiplicity of evaporated light particles considerably exceeds the multiplicity of preequilibrium particles in this energy range. In the proposed model, evaporation processes are taken into account in the following way. The introduction of phenomenological friction forces in the equations of motion (2.2) leads to a dissipation of part of the kinetic energy, whereby it is converted into the excitation energy of heavy fragments. Since the problem of how the excitation energy is shared among colliding nuclei has not yet been solved conclusively, we describe here the evaporation section of the spectrum, assuming that the total excitation energy is shared among colliding nuclei according to the simplest mechanism of equality of their temperatures, in which case the excitation energy is shared in proportion to the masses of the colliding nuclei. In the source rest frame, evaporated particles have a Maxwell distribution with respect to energy and an isotropic angular distribution. In the laboratory frame, the distribution of light fragments evaporated from the i th source has the form

$$f_i(\rho, E, \theta, \phi) = \frac{1}{2(\pi T_i(\rho))^{3/2}} \sqrt{E - V_C} \times \exp\left(-\frac{E - V_C + \varepsilon_i(\rho) - 2\sqrt{(E - V_C) \varepsilon_i(\rho)} \cos \theta'}{T_i(\rho)}\right). \quad (2.7)$$

Here, E is the laboratory energy of the light particle; V_C is the height of the Coulomb barrier for this particle in escaping from a heavy fragment; $\varepsilon_i(\rho) = mv_i^2(\rho)/2$, where m is the mass of the emitted light particle and v_i is the laboratory velocity of the i th evaporative heavy fragment; $T_i(\rho) = \sqrt{E_i^*(\rho)/a_i}$ is its temperature, where $E_i^*(\rho)$ is the fragment excitation energy; a_i is the level-density parameter in the corresponding nucleus; and $\cos \theta' = \sin \theta \sin \theta_i (\cos \phi \cos \phi_i + \sin \phi \sin \phi_i) + \cos \theta \cos \theta_i$, with (θ_i, ϕ_i) and (θ, ϕ) being the spherical angles of emission of, respectively, the i th hot fragment and the evaporated particle in the laboratory fragment. The quantities ε_i and T_i , as well as the angles θ_i and ϕ_i , are functions of the impact parameter ρ and are calculated by performing averaging over the total number of events at given ρ that have resulted in the formation of the i th fragment. The averaging of the function $f_i(\rho, E, \theta, \phi, \theta_i, \phi_i)$ over the azimuthal angle ϕ_i can be performed analytically, whereupon the dependence on the light-particle emission angle ϕ also disappears. In general, averaging over the polar angle θ_i of the heavy fragment can be performed only numerically. Within the model used here, three types of evaporated fragments can be formed. These are a projectile-like fragment (PLF), a targetlike fragment (TLF), and a compound nucleus (CN). In general, we therefore obtain three evaporation components of the energy spectrum of light particles. Within the model proposed here, the double-differential cross section for the formation of evaporated

light particles is calculated by the formula

$$\frac{d^2\sigma^{EV}}{dEd\Omega}(E, \theta) = \int_0^{\rho_{max}} 2\pi\rho[P_{CN}(\rho)C_{CN}f_{CN} + (1 - P_{CN}(\rho))(C_{PLF}f_{PLF} + C_{TLF}f_{TLF})]d\rho, \quad (2.8)$$

where $P_{CN}(\rho) = \Delta N_{CN}(\rho)/N_{tot}(\rho)$ is the probability of the formation of a compound nucleus in a collision occurring at an impact parameter ρ and C_i are constant normalization factors. These factors were introduced in order to normalize correctly the evaporation spectrum to experimental data; as a matter of fact, they are proportional to the measured value of the multiplicity of evaporated particles. The experimental normalization of the evaporation section of the spectrum of light particles makes it possible to single out their relative contribution to the total cross section, whereupon we can focus on preequilibrium light particles, which are the subject of our main interest.

§3. MECHANISMS OF PREEQUILIBRIUM LIGHT PARTICLE FORMATION

Within the proposed model, there are eight reaction channels contributing to the total cross section for the formation of preequilibrium light particles – fragments a or/and b . There are

$$(Aa) + (Bb) \rightarrow \begin{cases} A + a + B + b, \\ (Bb) + A + a, \\ (Aa) + B + b, \\ (Ab) + B + a, \\ (Ba) + A + b, \\ (AB) + a + b, \\ (ABb) + a, \\ (ABa) + b. \end{cases} \quad (3.1)$$

Our calculations revealed that, even at beam energies of about 30 MeV per nucleon, the main contribution to the cross section for light-particle formation comes from the breakup and breakup-transfer channels. Channels featuring a bound state of the heavy cores (ABx) contribute significantly only at low energies ($E_0 < 20$ MeV per nucleon).

From the scheme given by (3.1), it can be seen that the set of preequilibrium light particles can be broken down into two subsets including particles emitted from the projectile (particle a) and particles emitted from the target (particle b). Thus, three evaporation components of the energy spectrum of light particles are supplemented with two components of preequilibrium light particles. In just the same way as in the case of the evaporation spectra of light particles, it is necessary to introduce constant normalization factors for the preequilibrium target and the preequilibrium projectile component, since, in the four-body model used here, the multiplicity is

always less than or equal to two. The values of these factors were chosen in such a way that the calculated cross sections at the tails of the energy distributions would coincide in amplitude with experimental cross sections, since, in this region of the spectrum, only preequilibrium particles contribute.

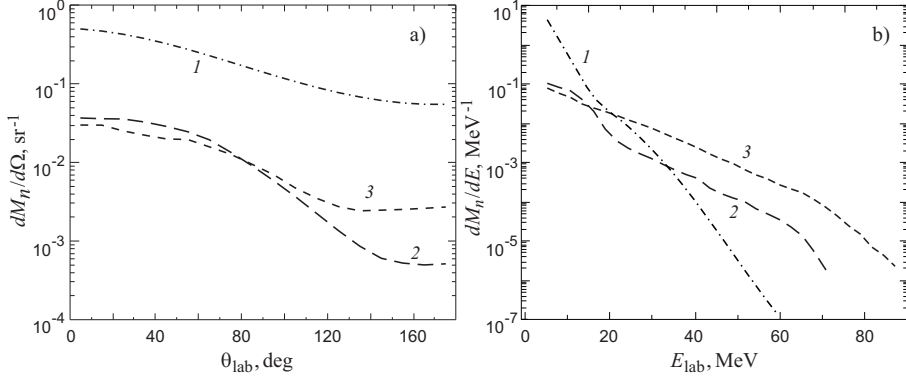


Fig. 1. Differential multiplicity of neutrons produced in $^{20}\text{Ne}(20 \text{ A MeV}) + ^{165}\text{Ho} \rightarrow n + X$ reactions versus (a) the neutron emission angles and (b) the neutron energy. Curves 1 represent the total contribution of evaporated neutrons, while curves 2 and 3 depict the contributions of preequilibrium neutrons emitted the projectile and the target, respectively.

As a first example, we applied the proposed model to studying the properties of neutrons emitted in $^{20}\text{Ne} + ^{165}\text{Ho} \rightarrow n + X$ reactions at a beam energy of $E_0 = 20 \text{ MeV}$ per nucleon. In this case, the target and the projectile nucleus are both represented as a bound state of a core and a neutron: $^{20}\text{Ne} = ^{19}\text{Ne} + n$ and $^{165}\text{Ho} = ^{164}\text{Ho} + n$. The binding energies of these systems were chosen on the basis of experimental data. Figure 1 shows the results of our calculations for the (a) angular and (b) energy distributions of neutrons for the above reaction. Curve 1 corresponds to equilibrium neutrons evaporated from PLF, TLF, and CN fragments of the reactions. Curves 2 and 3 represent the contributions of preequilibrium neutrons emitted from the projectile (particle *a*) and from the target (particle *b*), respectively.

In plotting the angular distribution displayed in Fig. 1a, integration of the differential multiplicity $d^2M_n/(dEd\Omega)$ with respect to energy was performed with the energy spectrum cut off in the low-energy section ($E_n > 5 \text{ MeV}$). It can be seen that the evaporation component is dominant over the entire angular range, both preequilibrium components being forward directed to a considerable extent.

As can be seen from Fig. 1b, it is the preequilibrium components (curves 2 and 3) that make a dominant contribution to the energy distribution at high neutron energies (at their velocities higher than the velocity of beam particles). That the hardest part of the spectrum corresponds to neutrons emitted from the target nucleus (and not from the projectile nucleus, as has usually been assumed so far) is a remarkable fact, which could not be anticipated from the outset. There is a simple explanation of this phenomenon, which is quite unusual at first glance.

Under the assumption that the core masses are much greater than the neutron mass, we will now calculate the maximum possible values that kinematics allows

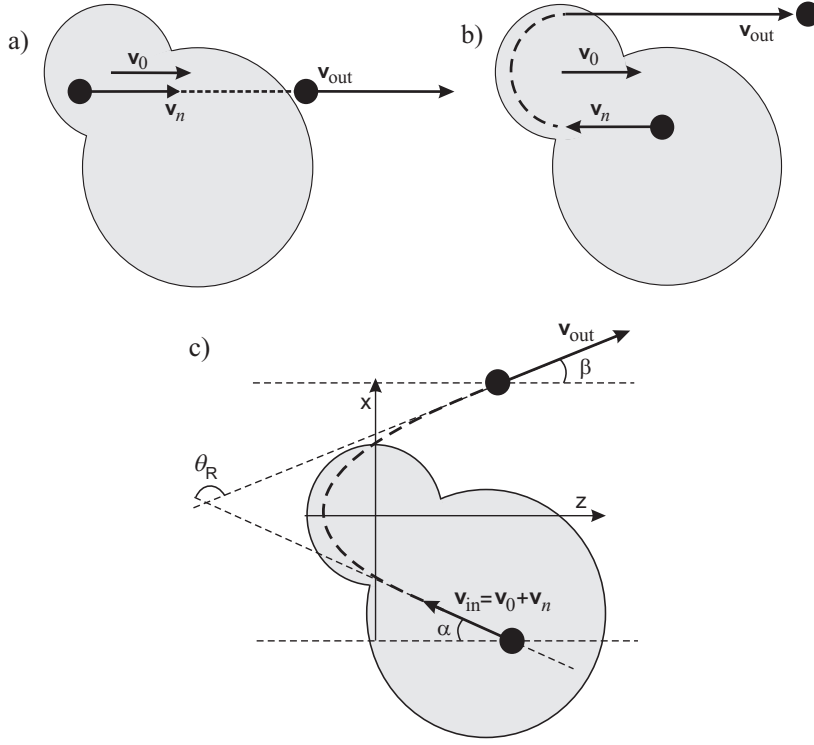


Fig. 2. Schematic representation of preequilibrium nucleon formation in a nucleus-nucleus collision: (a) emission of a nucleon from the projectile, (b) acceleration of a nucleon under the conditions of orbiting in the projectile field (this is equivalent to scattering on a moving reflecting wall), and (c) general case of nucleon emission from the target in projectile rest frame (for the notation, see main body of the text).

for the energy of neutrons emitted from the projectile and from the target. In doing this, we disregard the neutron-neutron interaction and the distortion of the trajectories of the heavy fragments A and B . The velocity of the projectile neutron in the laboratory frame (see Fig. 2a) is equal to the sum of the beam-particle velocity \vec{v}_0 ($E_0 = m_n v_0^2/2$) and the velocity of the internal motion of the neutron in the mean field \vec{v}_n of the projectile nucleus (in the case of a square well, we have $m v_n^2/2 - U_0 = -E_{sep}$). Thus, the projectile nucleon emitted from a nucleus-nucleus collision has the energy

$$\begin{aligned} E_n &= \left(\frac{m}{2} (\vec{v}_0 + \vec{v}_n)^2 - U_0 \right) \Big|_{v_n=v_F, \theta_n=0^\circ} \\ &= \frac{m}{2} (v_0^2 + 2v_0 v_F) - E_{sep}, \end{aligned} \quad (3.2)$$

where m is the neutron mass, U_0 is the depth of the mean field V_{Aa} , E_{sep} is the neutron-separation energy, and v_F is the Fermi velocity of projectile nucleons. If, for example, $v_0 \sim v_F$ and $E_0 \gg E_{sep}$, the maximum energy of the emitted nucleon is $E_n^{max} \sim 3E_0$. This mechanism of fast-light-particle formation was comprehensively investigated in ^{25), 29)}.

The mechanism responsible for the formation of high-energy neutrons from the target is more complicated. The main role in this process is played by the potential of the interaction between the projectile nucleus A and the target neutron b . Let us first consider a simplified model where the interaction V_{Ab} is replaced by the interaction of neutron b with an infinitely heavy moving wall. Suppose that b moves at a velocity v_n toward the core A , which, in turn, has a velocity v_0 directed oppositely. In their c.m. frame, the neutron velocity is $(v_0 + v_n)$; after an elastic collision, the neutron acquires the velocity $-(v_0 + v_n)$, which corresponds to the velocity $v_{out} = (2v_0 + v_n)$ in the laboratory frame. Under the condition that the internal-motion velocity of the target neutron, v_n , is equal to the Fermi velocity v_F , its asymptotic energy is

$$\begin{aligned} E_n|_{v_n=v_F, \theta_n=0^\circ} &= \frac{m}{2}(2v_0 + v_F)^2 - U_0 \\ &= 2m(v_0^2 + v_0v_F) - E_{sep}, \end{aligned} \quad (3.3)$$

where U_0 is the depth of the mean field V_{Bb} and is the energy of target-neutron separation. At $v_0 \sim v_F$ and $E_0 \gg E_{sep}$, the maximum energy is thus $E_n^{max} \sim 8E_0$, which is 2.5 times as great as the corresponding limit for neutrons emitted from the projectile.

The elastic scattering of neutrons at an angle of $\theta_{cm} = -180^\circ$ in the attractive mean field of the projectile nucleus is kinematically equivalent to their reflection from a repulsive wall (see Fig. 2b). The scattering of neutrons at such large angles ($\theta_{cm} < -180^\circ$), which is actually an orbiting process, is possible only at comparatively low neutron energies. At c.m. energies of $E_0 \geq AE_F \sim 40$ A MeV, neutrons can be deflected by the mean field ($U_0 \sim 50$ MeV) by not more than at a limiting negative angle θ_R that is referred to as the rainbow-scattering angle. By virtue of this, the maximum energy of neutrons emitted from the target depends strongly on the projectile energy, on the interaction potential V_{Ab} , on the neutron binding energy in the target, and on the friction forces. Disregarding the effect of neutrons on the motion of heavy fragments, assuming that the neutron acquires the maximum energy upon scattering by the projectile at the angle θ_R in the neutron-projectile c.m. frame (see Fig. 2c), and setting the initial neutron velocity in the target to the relevant Fermi velocity, we can estimate the asymptotic neutron energy (at $v_n = v_F$) as

$$\begin{aligned} E_n &= m \left(v_0^2 + v_0v_F \cos \alpha \right. \\ &\quad \left. + v_0 \cos \beta \sqrt{v_0^2 + v_F^2 + 2v_0v_F \cos \alpha} \right) - E_{sep} \end{aligned} \quad (3.4)$$

where α is the angle at which the neutron is incident on the target in the reference frame comoving with the target and β is the emission angle in the same reference frame (see Fig. 2c). The two angles are related to each other through the nuclear-rainbow-scattering angle, for which there is the empirical relation³⁴⁾

$$\theta_R = \left(V_C - 0.56U_0\sqrt{R_V/a_V} \right) / E_{cm} = - \left| \pi - \alpha - \beta \right|, \quad (3.5)$$

where V_C is the height of the Coulomb barrier (it is equal to zero for a neutron), while U_0 , R_V , and a_V are, respectively, the depth, the range, and the diffuseness of the interaction potential V_{Ab} . It turned out that the empirical formula (3.5), with the coefficient 0.56, agrees poorly with the exact classical calculation of the angle θ_R for the scattering of light particles (such as a proton or a neutron) on nuclei; therefore, we use here the coefficient 0.7. It can be seen that, at $\alpha = \beta = 0$ (that is, at $\theta_R = -180^\circ$), formula (3.4) reduces to (3.3).

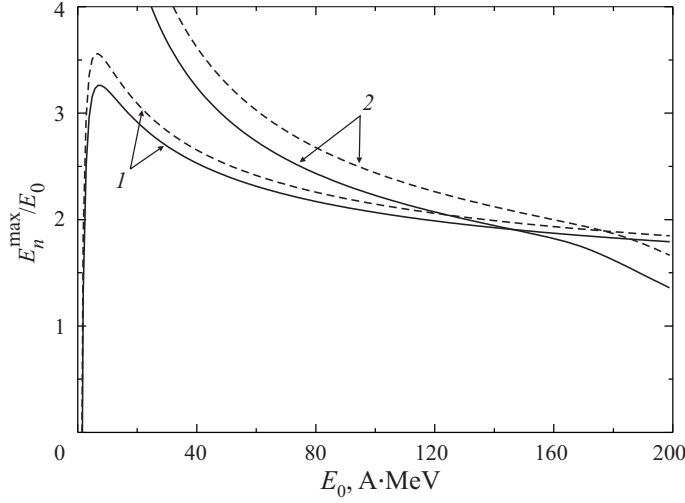


Fig. 3. The maximum energy E_n^{max} of preequilibrium neutrons as a function of the incident-beam energy E_0 for (solid curves) $^{20}\text{Ne} + ^{165}\text{Ho} \rightarrow n + X$ and (dashed curves) $^{165}\text{Ho} + ^{165}\text{Ho} \rightarrow n + X$ according to the calculations based on formulas (3.2) and (3.4). Curves 1 correspond to the maximum energy of neutrons emitted from the projectile, while curves 2 represent the energies of neutrons emitted from the target.

The maximum energies of preequilibrium neutrons originating from (solid curves) $^{20}\text{Ne} + ^{165}\text{Ho}$ and (dashed curves) $^{165}\text{Ho} + ^{165}\text{Ho}$ interactions are displayed in Fig. 3 versus the beam energy E_0 . Curves 1 correspond to the results obtained by calculating, on the basis of (3.2), the maximum energy of neutrons emitted from the projectile; curves 2 represent the energies of neutrons emitted from the target, their values being calculated by formula (3.4). From Fig. 3, it can be seen that, at energies below 100 MeV per nucleon, the fastest neutrons are emitted from the target and that, upon going over to the heavier projectile, the maximum energy of the emitted neutron becomes higher. This is because the range of the potential V_{Ab} increases, which entails an increase in the absolute value of the rainbow-scattering angle θ_R [see (3.5)].

Thus, an experimental investigation of reactions where projectiles different in mass are incident on the same target may be one of the tests of validity of conclusions that we have drawn. For nucleons emitted from the target and the projectile to be unambiguously identified, it is necessary that the spectrum of the projectile nucleons change insignificantly upon going from one system to another. In this case, the distinction between the distributions of preequilibrium nucleons will be deter-

mined completely by the yield of precisely target nucleons. In order to ensure the invariability of the spectra of preequilibrium nucleons emitted from the projectile, it is necessary to select projectile nuclei with similar features (such as the angular momentum of valence nucleons and the energies of their separation).

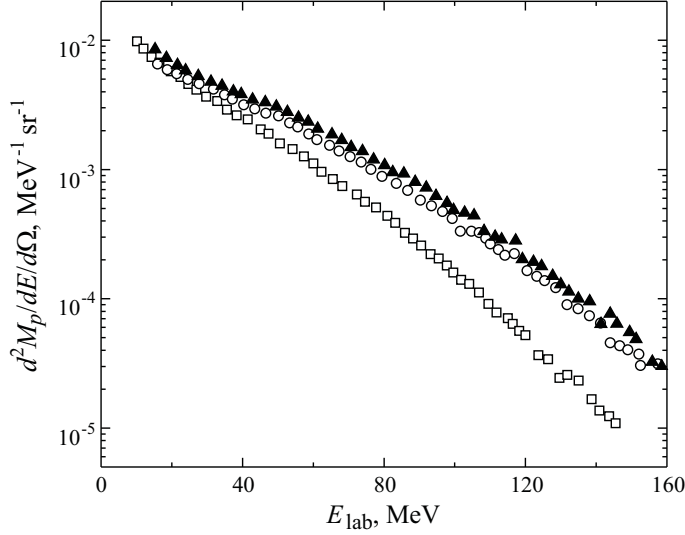


Fig. 4. Measured differential multiplicities of protons emitted at an angle of $\theta_{lab} = 51^\circ$ in (open boxes) $^{40}\text{Ar} + ^{51}\text{V} \rightarrow p + X$, (open circles) $^{132}\text{Xe} + ^{51}\text{V} \rightarrow p + X$, and (closed triangles) $^{132}\text{Xe} + ^{197}\text{Au} \rightarrow p + X$ interactions at a beam energy of 44 MeV per nucleon¹⁶⁾.

Figure 4 shows the measured differential multiplicities of protons originating at an angle of $\theta_{lab} = 51^\circ$ from $^{40}\text{Ar} + ^{51}\text{V} \rightarrow p + X$, $^{132}\text{Xe} + ^{51}\text{V} \rightarrow p + X$, and $^{132}\text{Xe} + ^{197}\text{Au} \rightarrow p + X$ interactions at a beam energy of 44 MeV per nucleon¹⁶⁾. It can be seen that, upon going over from the projectile nucleus of ^{40}Ar to the heavier species of ^{132}Xe , the slope of the proton spectrum decreases, which corresponds to an increase in the yield of fast light particles. On the contrary, the replacement of the target nucleus causes virtually no changes in the energy distribution of protons. The change in the character of the spectra in response to going over from one projectile-nucleus species to another can hardly be explained by different properties of the projectile species, because the internal structure of the projectile (the height of the Coulomb barrier, the binding energy, shell effects, etc.) does not have a significant effect on the properties of preequilibrium protons at the high beam energies considered here. Moreover, the mechanism of light-particle emission from the projectile nucleus is independent of its mass—only the multiplicity of light particles (that is, the absolute normalization of their spectrum) depends on it. The effect of dissipative forces, which directly depend on the target-nucleus mass, leads to a moderation of protons emitted from the projectile nucleus. It follows that the use of a heavier target nucleus would lead to a decrease in the yield of fast protons (because of the intensification of dissipative processes) if they were formed only via stripping from the target. However, a comparison of the data presented in Fig. 4 for $^{132}\text{Xe} (44 \text{ A MeV}) + ^{51}\text{V}$, ^{197}Au interactions does not reveal any significant

change in the proton spectra. Nonetheless, the above mechanism of the acceleration of target nucleons in the mean field of the projectile is very sensitive to the geometric dimensions of the the projectile (that is, to its mass). Thus, we can conclude that the main contribution to the high-energy section of the spectra displayed in Fig. 4 comes precisely from protons emitted from the target and accelerated by the mean field of the projectile. The conclusion that the energy spectrum of protons depends weakly on the choice of target nucleus also follows from the data presented by Jasek et al.¹⁰⁾, who studied the target-mass dependence of the yields of various products (including protons) from the reactions induced by $^{40}\text{Ar} + ^{197}\text{Au}$ and $^{40}\text{Ar} + ^{40}\text{Ca}$ collisions at an energy of $E_0 = 42$ MeV per nucleon.

Within our model, we will now consider the effect of nucleon-nucleon collisions on the formation of fast light particles. Suppose that, in the laboratory frame, a target nucleon has a velocity \vec{v}_j prior to a collision event; the velocity of a projectile nucleon is equal to the sum of the beam-particle velocity \vec{v}_0 and the nucleon velocity \vec{v}_i within the projectile. One of the nucleons can acquire the maximum velocity if, upon the collision event, it carries away the entire amount of the relative-motion energy. In this case the maximum energy of the emitted nucleon is ($i = a, b$)

$$E_i^{max} = \frac{m}{2} (v_b^2 + (v_0 + v_a)^2) - \frac{mv_i^2}{2} - E_i^{sep}. \quad (3.6)$$

From (3.6), it follows that, if $v_0 \sim v_i \sim v_F$, then $E_i^{max} \sim 4E_0$. For $^{20}\text{Ne} + ^{165}\text{Ho} \rightarrow n + X$ reactions, Fig. 5 displays the maximum neutron energy as a function of the beam energy according to the calculations based on formulas (3.2) (curve 1), (3.4) (curve 2), and (3.6) (curve 3). It can be seen that, over the entire energy range, nucleon-nucleon collisions in this reaction can in principle lead to the formation of yet more energetic light particles in relation to the first two mechanisms considered above.

In actual experiments, the boundaries depicted by the curves in Fig. 5 will be smeared because of the high-energy component of the momentum distributions in the projectile and the target nucleus ($v_n > v_F$); in the case corresponding to curve 3, there is also the contribution to this smearing from the Pauli exclusion principle, which forbids nucleons that suffered a collision to occur in states already occupied by other intranuclear nucleons, with the result that the probability of the acceleration of nucleons to the maximum possible degree is considerably suppressed.

Let us introduce a nucleon-nucleon interaction featuring a repulsive core at short distances. Solving the set of Eqs. (2.2) for initial conditions chosen at random, we can determine numerically the maximum energy acquired by a nucleon upon a nucleon-nucleon collision in the mean field of the relevant dinuclear system. Testing, in the output channels, the binding energy of the recoil nucleon, we can also take into account the Pauli exclusion principle in our calculations. The results of our calculations for $^{20}\text{Ne} + ^{165}\text{Ho} \rightarrow n + X$ reactions versus E_0 are shown in Fig. 5 by points. It can be seen that, at low initial energies ($E_0 \sim 20$ MeV per nucleon), the Pauli exclusion principle has a crucial effect on the formation of fast preequilibrium neutrons in nucleon-nucleon collisions. In this case, the energy of the emitted particles does not exceed $3.5E_0$. At higher values of the beam energy E_0 , the dis-

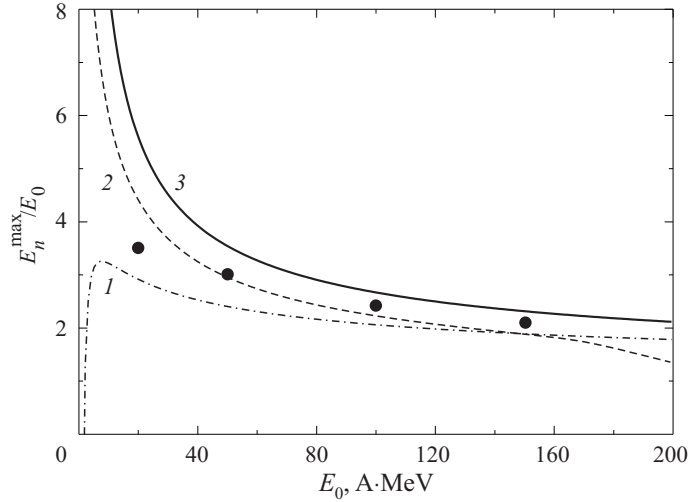


Fig. 5. Maximum energy of preequilibrium neutrons originating from $^{20}\text{Ne} + ^{165}\text{Ho} \rightarrow n + X$ reactions as a function of the beam energy. Curves 1 and 2 represent the data analogous to those depicted by the corresponding curves in Fig. 3. Curve 3 corresponds to the maximum energy acquired by the neutron upon an elastic nucleon-nucleon collision in the mean field of the relevant dinuclear system (according to the calculation by formula (3.6) not allowing for the Pauli exclusion principle). The points represent the results obtained with allowance for the Pauli exclusion principle (for details, see main body of the text).

crepancy between the predictions of formula (3.6) and the results of the calculation decreases gradually. It should be noted that the maximum energy of neutrons was calculated with allowance for dissipative forces acting between the heavy cores and exerting, as will be shown below, a pronounced effect on the spectra of preequilibrium light particles. The dissipative forces moderate the projectile nucleus; that is, they reduce the velocity v_0 . This leads to an additional decrease in the quantity E_n^{max} in nucleon-nucleon collisions. With increasing initial energy E_0 , the effect of dissipative forces becomes less pronounced, since the valence nucleon does not have time to "experience" the moderating influence of the projectile mean field. Thus, we can conclude that, up to beam energies of $E_0 \sim AE_F$, the role of nucleon-nucleon collisions is less significant than the role of the mean fields. At higher beam energies, the maximum energy acquired by nucleons as the result of nucleon-nucleon collisions becomes greater than the energy of target nucleons accelerated by the projectile mean field.

§4. COMPARISON WITH EXPERIMENTAL DATA

In order to verify the qualitative conclusions drawn in the preceding section, we have analyzed the differential cross sections for the yield of neutrons and protons from a few nuclear reactions and performed a comparison with available experimental data.

The double-differential cross sections measured in ¹⁵⁾ for the yield of neutrons

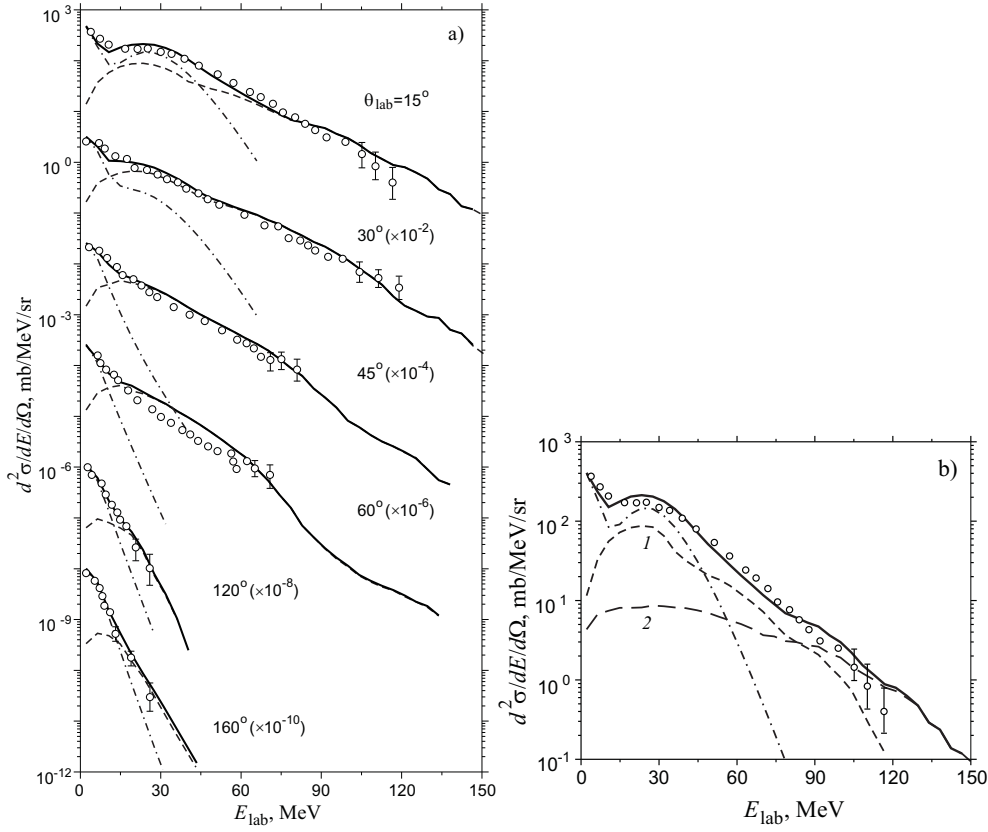


Fig. 6. (a) Measured and calculated differential cross sections for neutron formation in $^{36}\text{Ar}(35 \text{ A MeV}) + ^{107}\text{Ag} \rightarrow n + X$ reactions: (points) experimental data from ¹⁵⁾, (dash-dotted curves) contribution of evaporated neutrons, (dashed curves) total contribution of preequilibrium neutrons emitted from the projectile and the target, and (solid curves) sum of the evaporation and the preequilibrium component; (b) theoretical results for the single angle of $\theta_{lab} = 15^\circ$ that are basically the same as in Fig. 6a, except that the contribution to the differential cross section from neutrons emitted (curve 1) by the projectile and (curve 2) by the target are shown individually instead of their total contribution.

from $^{36}\text{Ar}(35 \text{ A MeV}) + ^{107}\text{Ag} \rightarrow n + X$ reactions are displayed in Fig. 6a, along with the results of the relevant calculations. The dash-dotted, the dashed, and the solid curve represent, respectively, the evaporation component, the preequilibrium component, and their sum. The equilibrium part of the spectrum receives contributions from neutrons evaporated by a targetlike fragment (this is the isotropic low-energy component completely saturating the evaporation spectrum at large angles) and from neutrons evaporated by a projectile-like fragment, the maximum in the distribution corresponding to forward angles and energies close to the beam energy.

Figure 6b gives a more detailed pattern for the contribution of preequilibrium neutrons emitted from (curve 1) the projectile and (curve 2) the target at an angle of $\theta_{lab} = 15^\circ$. The solid and the dash-dotted curve are identical to their counterparts in Fig. 6a. It can be seen that the hardest section of the spectrum is associated with

neutrons emitted from the target nucleus. For intermediate values of the emission angle ($\theta_{lab} < 90^\circ$), this trend is conserved; only in the region of large angles are the contributions of the two preequilibrium components approximately equal.

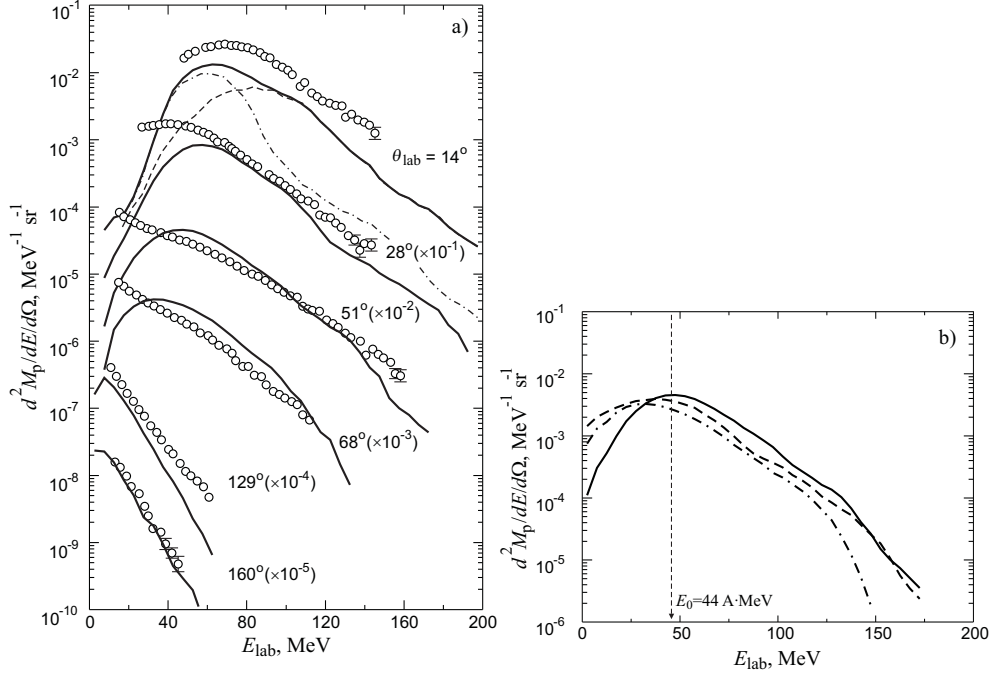


Fig. 7. (a) Comparison of (points) the measured¹⁶⁾ and (solid curves) the calculated differential multiplicity of preequilibrium protons formed in ^{132}Xe (44A MeV) + $^{197}\text{Au} \rightarrow p + X$ reactions. The dashed and the dash-dotted curve represent the contributions of preequilibrium protons emitted at an angle of $\theta_{lab} = 14^\circ$ from the target and the projectile, respectively. The contribution of evaporated protons is not shown. (b) Calculated differential multiplicities of protons emitted at an angle of $\theta_{lab} = 51^\circ$ in (solid curve) $^{132}\text{Xe} + ^{197}\text{Au} \rightarrow p + X$, (dashed curve) $^{132}\text{Xe} + ^{51}\text{V} \rightarrow p + X$, and (dash-dotted curve) $^{40}\text{Ar} + ^{51}\text{V} \rightarrow p + X$ reactions at the beam energy of 44 MeV per nucleon.

Figure 7a displays experimental data from¹⁶⁾ on the differential multiplicity of protons emitted in $^{132}\text{Xe}(44 \text{ A MeV}) + ^{197}\text{Au} \rightarrow p + X$ reactions. In that figure, the solid curves represent the calculated energy distribution of preequilibrium protons; shown additionally for the emission angle of $\theta_{lab} = 14^\circ$ are the contributions of protons escaping from (dashed curve) the target and (dash-dotted curve) the projectile. The contribution of evaporated protons is not presented. The theoretical results for the proton spectrum at $\theta_{lab} = 14^\circ$ noticeably underestimate the experimental cross section in magnitude, but they reproduce quite well the behavior of experimental data. On the contrary, the theoretical curves in the region of backward angles ($\theta_{lab} = 129^\circ, 160^\circ$) lie somewhat above the experimental data on the differential multiplicity of preequilibrium protons. This is because the evaporation component must be dominant in this region. We can see that, despite the use of quite a simple semiclassical model, the agreement with experimental data is by and large satisfactory.

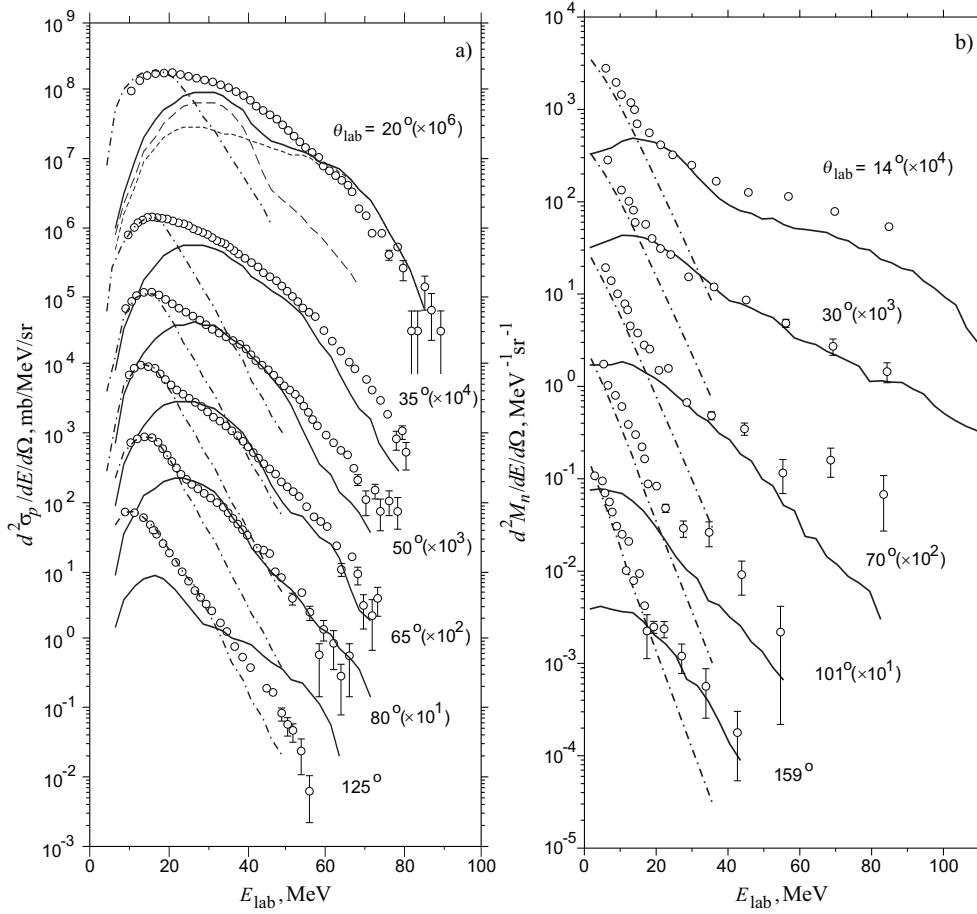


Fig. 8. (a) Measured⁴⁾ and calculated double-differential cross sections for proton production in $^{16}\text{O}(20 \text{ A MeV}) + ^{197}\text{Au} \rightarrow p + X$ reactions and (b) measured⁸⁾ and calculated differential multiplicities of neutrons from $^{20}\text{Ne}(30 \text{ A MeV}) + ^{165}\text{Ho} \rightarrow n + ER$ ($\theta_{ER} = 5.6^\circ$) reactions: (solid curves in Figs. 8a and 8b) computed distributions of preequilibrium protons and neutrons, respectively; (dash-dotted curves) contribution to the distributions from evaporated light particles; and (points) experimental data. In Fig. 8a, the contributions of preequilibrium protons emitted from the projectile and from the target at an angle of $\theta_{lab} = 20^\circ$ are shown individually by long and short dashes, respectively.

Figure 7b shows the computed energy distributions of preequilibrium protons emitted at an angle of $\theta_{lab} = 51^\circ$ in (solid curve) $^{132}\text{Xe} + ^{197}\text{Au} \rightarrow p + X$, (dashed curve) $^{132}\text{Xe} + ^{51}\text{V} \rightarrow p + X$, and (dash-dotted curve) $^{40}\text{Ar} + ^{51}\text{V} \rightarrow p + X$ reactions at a beam energy of 44 MeV per nucleon. It can be seen that, in the region of high energies, the spectrum of product protons is harder for the heavier projectile of ^{132}Xe than for the lighter projectile of ^{40}Ar owing to particles emitted from the target nucleus. No such effect arises upon replacing the target nucleus by a heavier one. Comparing the curves in Fig. 7b with the experimental data in Fig. 4, we can see that the agreement between the results of the theoretical calculations and the experimental data is quite satisfactory.

In Fig. 8a, the double-differential cross section measured in⁴⁾ for proton formation in $^{16}\text{O}(20\text{A MeV}) + ^{197}\text{Au} \rightarrow p + X$ reactions is contrasted against the results of the theoretical calculations based on the model employed here. The solid curves correspond to the total contribution of preequilibrium protons emitted from the target and the projectile. The dash-dotted curves represent the contribution of evaporated protons. For protons emitted at an angle of $\theta_{lab} = 20^\circ$, more detailed dependences are shown individually for protons escaping from (long dashes) the projectile and (short dashes) the target. The cross sections calculated for the reactions in question agree well with experimental data at small and intermediate values of the emission angle. As in the preceding case, however, the cross section is overestimated at large values of the proton emission angle.

In Ref.⁸⁾, the differential multiplicity was measured for neutron formation in coincidence with the evaporation residue in the reaction $^{20}\text{Ne}(30\text{A MeV}) + ^{165}\text{Ho} \rightarrow n + ER(\theta_{ER} = 5.6^\circ)$. Within the model used here, we can calculate the differential multiplicity of neutrons in coincidence with the evaporation residue, taking, however, no account of its emission angle θ_{ER} . This limitation is due to the fact that we can only roughly estimate the contribution of evaporation processes to the cross section for the formation light fragments; in doing this, we underestimate the multiplicities of preequilibrium particles, so that we cannot calculate precisely the emission angle for the evaporation residue. In Fig. 8b, the multiplicities calculated in the present study are contrasted against the experimental data from⁸⁾. In that figure, the dash-dotted curve represents the total contribution of evaporated neutrons, while the solid curve corresponds to the total distribution of preequilibrium neutrons. At some values of the emission angle, there is a sizable discrepancy between the results of theoretical calculations and experimental data in the region of high energies. In all probability, this is due to imperfections of the model in dealing with correlation experiments, which require a precise treatment of the statistical decay of an excited nucleus. By and large, we can state that, despite the simplicity of the proposed model, there is good agreement, in the energy range being considered, between the calculated cross sections for the yield of light particles from nucleus-nucleus collisions and relevant experimental data.

§5. DYNAMICS OF LIGHT-PARTICLE FORMATION AND ROLE OF DISSIPATIVE FORCES

In treating the dynamics of nucleus-nucleus collisions on the basis of the semi-classical approach involving two-particle interactions, there remains an ambiguity in choosing the parameters of these interactions. In assessing the parameters of the potentials that simulate the interaction between a light particle and a heavy fragment, we relied here on experimental data obtained by exploring elastic scattering and on the results of their treatment within the optical model³¹⁾. It is well known, however, that the optical model leads to a discrete and a continuous ambiguity in the potential parameters. In the present calculations, these parameters were therefore varied within 10 – 20% in order to determine the stability of the results of these calculations and conclusions drawn from them. In particular, the potentials V_{Aa} and

V_{Bb} (that is, the interaction of a valence nucleon with a nuclear core) chosen in the Woods-Saxon form had the parameters of $U_0 = 50 - 60$ MeV, $r_0 = 1.15 - 1.25$ fm, and $a_v = 0.45 - 0.6$ fm. Variations of these parameters in the above ranges do not have a strong effect on the angular and energy distributions of preequilibrium light particles.

The potentials V_{Ab} and V_{Ba} play a much more significant role. As was shown above, the former is responsible for the acceleration of the target valence nucleon and, as a consequence, for the formation of the spectrum of preequilibrium light particles emitted from the target. The latter determines the angular distribution of light particles emitted by the projectile. The parameters of the potential V_{Ab} specify the rainbow-scattering angle in (3.5), which sets a kinematical limit on the energy of the emitted light particle b . In the calculations, the parameters of these potentials for various nuclei were taken in the following ranges: $U_0 = 45 - 55$ MeV, $r_0 = 1.15 - 1.25$ fm, and $a_V = 0.45 - 0.65$ fm.

In addition to the real parts of the potentials V_{Ab} and V_{Ba} , we also introduced imaginary parts (see Section 2). It turned out that these imaginary parts, which determine the absolute values of the cross sections, have virtually no effect on other observables, such as the slope of the spectrum and the position of the maximum. In the case being considered, the imaginary parts of the potentials V_{Ab} and V_{Ba} , were chosen in the Woods-Saxon form with parameters based on data from Ref. ³¹).

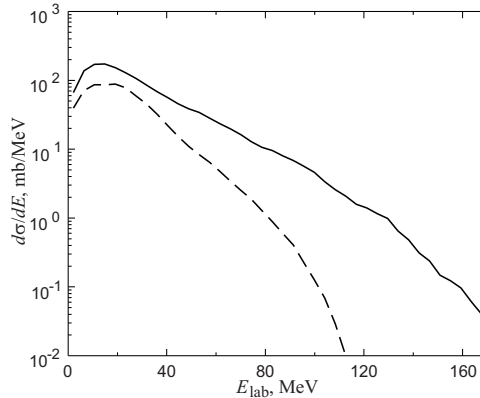


Fig. 9. Differential cross section for preequilibrium neutrons originating from $^{36}\text{Ar}(35 \text{ A MeV}) + ^{107}\text{Ag} \rightarrow n + X$ reactions for impact-parameter values from the intervals (dashed curve) $\rho \in [0,4]$ fm and (solid curve) $\rho \in [4,9]$ fm.

The potential V_{AB} simulating the nucleus-nucleus interaction plays a significant role in the formation of light particles at low beam energies of $E_0 < 20$ MeV per nucleon, but it becomes less important as the beam energy increases. The potential V_{AB} determines the trajectories of the projectile, which is responsible for the acceleration of target nucleons. That the projectile moves along trajectories not coinciding with a straight line smears the region of forward angles in the spectrum of the fastest light particles. Such particles are produced in peripheral collisions characterized by impact-parameter values close to that of tangential collision. Figure 9 shows the differential distribution of the cross section with respect to energy

for preequilibrium neutrons originating from $^{36}\text{Ar}(35 \text{ A MeV}) + ^{107}\text{Ag}$ interactions at impact-parameter values from various ranges. The dashed curve represents the results for impact parameters satisfying the condition $\rho < 4 \text{ fm}$, while the solid curve corresponds to ρ values between 4 and 9 fm. In the case of a tangential collision, the impact parameter is about 8.5 fm. From Fig. 9, it can be seen that the main contribution to the cross section comes from events where the impact parameter is large (solid curve). Therefore, the cross section for the yield of the most energetic light particles from nuclear reactions is governed primarily by the dynamics of peripheral collisions, which in turn depends on the nuclear component of the interaction potential V_{AB} .

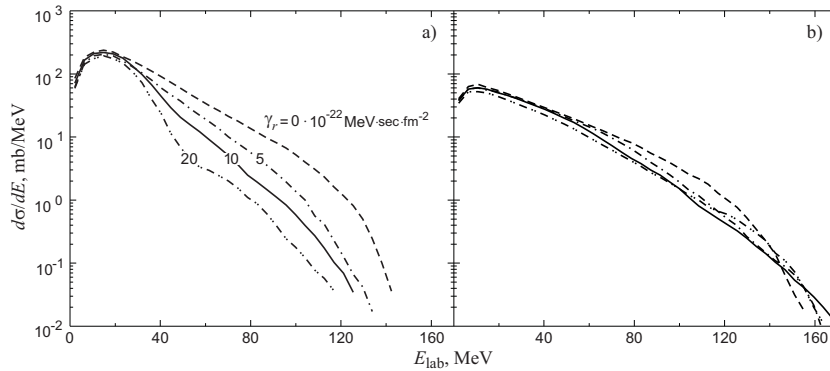


Fig. 10. Differential cross sections calculated for preequilibrium neutrons emitted by (a) the projectile and (b) the target in $^{36}\text{Ar}(35 \text{ A MeV}) + ^{107}\text{Ag} \rightarrow n + X$ reactions. Different curves correspond to different values of the radial coefficient of friction γ_r . The values of this coefficient in $10^{-22} \text{ MeV s fm}^{-2}$ units are indicated on each curve in Fig. 10a.

As was demonstrated above, the relative velocity of the light particle from the target and the heavy projectile core determines the maximum angle [see Eq. (3.5)] at which the light particle can be scattered and, hence, the maximum energy of this particle. At beam energies E_0 of about the Fermi energy, the relative velocities are so great that the angle at which the light particle is scattered is small, and so is therefore its energy. On the other hand, it is well known from experiments that, in the hard section of the spectrum, the energy of light particles can be as large as about $4E_0$ to $6E_0$. The inclusion of nuclear friction in the model being considered is a mechanism that could ensure the reduction of the relative velocity in the scattering of the light fragment b on the projectile core A . As was indicated above, we introduce only the forces of friction between the cores of the projectile and the target. The form factor of dissipative forces is not known precisely; therefore, use was made here of a phenomenological form factor of the Fermi type both for the radial and for the tangential component. In³³⁾, it was indicated that, at the same values of the coefficient of friction, a form factor of this type leads to identical friction between two light and two heavy nuclei at equal distances between their surfaces. This means that, in this case, the coefficients of friction must depend on the masses of colliding nuclei; therefore, one cannot expect that there exist universal values of these coefficients for any nuclear system.

For preequilibrium neutrons originating from $^{36}\text{Ar}(35 \text{ A MeV}) + ^{107}\text{Ag} \rightarrow n + X$ reactions, we have calculated the formation cross sections at various values of the radial coefficient of friction. In Fig. 10, the results of these calculations are presented individually for neutrons emitted by (a) the projectile and (b) the target. From Fig. 10a, it can be seen that nuclear friction exerts the strongest effect on the cross section for the yield of projectile neutrons. The dissipation of energy leads to a decrease in the relative velocity v_0 of the nuclei and, hence, to a reduction of the maximum energy of neutrons emitted by the projectile [see Eq. (3·2)]. For particles emitted from the target, an increase in the coefficients of friction leads, however, to an increase in their maximum energy (by 10 to 15 MeV in the case being considered) owing to a decrease in the energy of the relative motion of the target neutron and the projectile and, consequently, owing to the growth of the angle of rainbow neutron scattering in the field of the projectile [see Eqs. (3·4), (3·5)]. That the form of the energy spectrum of neutrons escaping from the target shows a relatively weak dependence on dissipative nuclear forces is explained predominantly by the peripheral character of processes leading to neutron emission. Needless to say, an indefinite increase in the coefficient of friction would not lead to a steady growth of the maximum energy of neutrons escaping from the target-in other

Fixing the initial configurations of the projectile and the target nucleus, the collision energy E_0 , and the impact parameter ρ , we can single out, from the entire set of events, the following two subsets: one comprising events where the light particle is emitted from the projectile and the other comprising events where the light particle is emitted from the target. The initial parameters can be chosen in such a way that the process of light-particle formation in each of these subsets would be affected predominantly by any mechanism of those that were described in Section 3. By varying the parameters of nuclear friction for each of these event types, one can investigate their effect on collision dynamics and on the properties of the emitted light particle - that is, on its energy and emission angle. Such an analysis was performed in this study for preequilibrium neutrons originating from $^{36}\text{Ar}(35 \text{ A MeV}) + ^{107}\text{Ag}$ interaction. As was anticipated, the asymptotic energy of target neutrons accelerated by the mean field of the projectile nucleus grows as the coefficient γ_r is increased up to $(15\text{-}20) \times 10^{-22} \text{ MeV s fm}^{-2}$. A further increase in γ_r leads to a fast reduction of the neutron energy. The neutron emission angle in the laboratory frame decreases with increasing radial coefficient of friction. Thus, we can state that small friction as it focuses preequilibrium light particles from the target in the beam direction and leads to the growth of their energy. With increasing γ_r , the energy of a neutron emitted by the projectile nucleus decreases monotonically, while its emission angle grows in absolute value, remaining negative. This means that, when the velocity of the relative motion of the nuclei involved is reduced because of the effect of dissipative forces, the projectile neutron is subjected, for a longer time, to the effect of the attracting target field, which, as the coefficient γ_r is increased, distorts its trajectory ever more strongly and which, in the case of strong nuclear friction, can even lead to neutron capture by the target. Therefore, the effect of the growth of dissipative forces on light particles emitted from the projectile is opposite to the effect of the analogous growth on target light particles. We also note that the introduction of a

small friction does not affect the total cross section (that is, the total multiplicity) for the production of preequilibrium light particles, changing only the character of the differential cross section as a function of energy and emission angle; that is, this leads to a redistribution of emitted light particles in terms of the coordinates E_n and θ_n . And only in the case of large dissipative forces does the multiplicity of preequilibrium light particles decrease significantly. We can see that the properties of the angular and the energy distributions of light particles are sensitive to the form of dissipative nuclear forces; therefore, valuable information about the magnitude of the coefficients of nuclear friction and about other parameters of the dissipative function-in particular, about their dependence on the masses of colliding nuclei and on energy-can be extracted from an analysis of a vast body of experimental data on the yields of fast preequilibrium particles. By way of example, the friction-parameter values used in calculating the cross sections for the formation of light particles in Section 4 are given in the table. In each case, we have chosen a radial form factor of the Fermi type; its radius R_{fr} and its diffuseness parameter a_{fr} are also quoted in the table I.

Table I. Friction form-factor parameters

| Reaction | $\gamma_r,$ | | $\gamma_t,$ | | $R_{fr},$ fm | $a_{fr},$ fm |
|--|-------------|--------------------|-------------|--------------------|-----------------|-----------------|
| | 10^{-22} | MeV sec fm $^{-2}$ | 10^{-22} | MeV sec fm $^{-2}$ | | |
| ^{132}Xe (44 A MeV) + ^{197}Au | | 45 | | 0.4 | 13.1 | 0.7 |
| ^{20}Ne (30 A MeV) + ^{165}Ho | | 15 | | 0.1 | 9.4 | 0.7 |
| ^{36}Ar (35 A MeV) + ^{107}Ag | | 10 | | 0.1 | 9.3 | 0.7 |
| ^{16}O (20 A MeV) + ^{197}Au | | 6 | | 0.05 | 9.2 | 0.7 |

§6. CONCLUSION

In order to study intermediate-energy ($E_0 < 100$ MeV per nucleon) heavy-ion collisions leading to the production of fast light particles, we have proposed a classical four-body model. Within this model, projectile and target nuclei are represented as two-particle subsystems, each consisting of a heavy core and a light fragment (for example, a proton, a neutron, an alpha particle, etc.). The proposed approach has been used to study in detail the dynamics and the mechanisms of formation of preequilibrium light particles originating from $^{20}\text{Ne}(20, 30 \text{ A MeV}) + ^{165}\text{Ho} \rightarrow n + ER$, $^{16}\text{O}(20 \text{ A MeV}) + ^{197}\text{Au} \rightarrow p + X$, $^{36}\text{Ar}(35 \text{ A MeV}) + ^{107}\text{Ag} \rightarrow n + X$, $^{40}\text{Ar}(44 \text{ A MeV}) + ^{51}\text{V} \rightarrow p + X$, and $^{132}\text{Xe}(44 \text{ A MeV}) + ^{51}\text{V}, ^{197}\text{Au} \rightarrow p + X$ reactions treated by way of example. Our theoretical estimates agree well with experimental data.

The role of two-body interactions in the process of light-particle formation has been investigated in detail, and the main mechanisms of this process have been determined. It has been shown that the high-energy component in the spectrum of neutrons and protons from these reactions corresponds to preequilibrium particles emitted both by the projectile and by the target nucleus. It has been found that the yield of ultrafast preequilibrium light particles from the target nucleus exceeds the yield of light particles from the projectile nucleus, almost completely

saturating the hardest section of their energy spectrum. The process of target-nucleon acceleration by the projectile mean field plays a dominant role here. Nucleon-nucleon collisions are insignificant in this respect at energies below 50 MeV per nucleon. With increasing projectile energy, the effect of the mean fields weakens, whereas nucleon-nucleon collisions become a dominant process in the formation of the hard section of light-particle spectra.

It has been revealed that nuclear-friction forces strongly affect the character of the angular and energy distributions of preequilibrium light particles. At high energies, the introduction of dissipative forces leads, among other things, to a moderation of the projectile, with the result that the mean fields exert a more pronounced effect on the nucleons of colliding nuclei. The forces of friction reduce the yield of fast particles from the projectile nucleus, but they increase the maximum energy of light particles emitted by the target nucleus. More detailed information about the character and the magnitude of dissipative nuclear forces would be deduced from a comprehensive analysis of extensive experimental data on the cross sections for light-particle formation within this approach.

The proposed new mechanism of preequilibrium-light-particle formation (acceleration of target nucleons in the projectile mean field) is indirectly confirmed by experimental data. In order to obtain more compelling pieces of evidence in favor of the existence of this mechanism, one could, for example, study the spectra of neutrons or protons emitted in collisions of two different projectile species with the same target nucleus. In doing this, it is necessary to select the combinations of projectiles and targets in such a way that one could separate light particles emitted by the projectile nucleus from those emitted by the target nucleus. For this, it is required that the spectrum of light particles originating from the projectile change insignificantly upon going over from one projectile species to another. In this case, the change in the observed distribution of preequilibrium light particles will be completely determined by the change in the distribution of light particles emitted by the target.

References

- 1) R.M. Eisberg and G.Igo, Phys. Rev. **93** (1954), 1039.
- 2) R.M. Eisberg, Phys. Rev. **94** (1954), 739.
- 3) T.C. Awes et al., Phys. Rev. **C24** (1981), 89.
- 4) T. C. Awes et al., Phys. Rev. **C25** (1982), 2361.
- 5) T. C. Awes et al., Phys. Lett. **B103** (1981), 417.
- 6) J. Kasagi, Phys. Lett. **104B** (1981), 434.
- 7) B. Ludewigt et al., Phys. Lett. **108B** (1982), 15.
- 8) D. Hilscher et al., Nucl. Phys. **A471** (1987), 77c.
- 9) E. Holub et al., Phys. Rev. **C33** (1986), 143.
- 10) B. V. Jacak et al., Phys. Rev. **C35** (1987), 1751.
- 11) G. Lanzano et al., Phys. Rev. **C58** (1998), 281.
- 12) Yu. E. Penionzhkevich et al., Preprint No. E7-98-282, JINR (Dubna,1998).
- 13) D. Prindle et al., Phys. Rev. **C57** (1998), 1305.
- 14) P. Sapienza et al., Nucl. Phys. **A630** (1998), 215c.
- 15) D. Sackett et al., Phys. Rev. **C44** (1991), 384.
- 16) R. Alba et al., Phys. Lett. **B322** (1994), 38.
- 17) S. I. A. Garpman, D. Sperber, and M. Zielinska-Pfabe, Phys. Lett. **90B** (1980), 53.

- 18) T. Udagawa and T. Tamura, Phys. Rev. Lett. **45** (1980), 1311.
- 19) V. E. Bunakov, V. I. Zagrebaev, and A. A. Kolozhvari, Izv. Akad. Nauk SSSR **Ser. Fiz.** (44), 1980,2331.
- 20) V. I. Zagrebaev and A. Yu. Kozhin, Izv. Akad. Nauk SSSR **Ser. Fiz.** (52), 1988,104.
- 21) V. E. Bunakov and V. I. Zagrebaev, Z. Phys. **A333** (1989), 57.
- 22) V. I. Zagrebaev, Ann. Phys. (N.Y.) **197** (1990), 33.
- 23) V. I. Zagrebaev, in Proceedings of the First International School in Nuclear Physics, Kiev, 1990, p. 471.
- 24) S. Leray et al., Z. Phys. **A320** (1985), 383.
- 25) J. P. Bondorf et al., Nucl. Phys. **A333** (1980), 285.
- 26) K. Mohring, W. J. Swiatecki, and M. Zielinska-Pfabe, Nucl. Phys. **A440** (1985), 89.
- 27) F. Sebil and B. Remaud, Z. Phys. **A310** (1983), 99.
- 28) J. Randrup and R. Vanderbosch, Nucl. Phys. **A474** (1987), 219.
- 29) V. Zagrebaev, in Proceedings of the XV Nuclear Physics Divisional Conference LEND-95, St. Petersburg, 1995 (World Sci., Singapore, 1995), p. 457.
- 30) V. Zagrebaev and Yu. Penionzhkevich, Prog. Part. Nucl. Phys. **35** (1995), 575.
- 31) C. M. Perey and F. G. Perey, At. Data Nucl. Data Tables **13** (1974), 293.
- 32) J. Blocki, J. Randrup, W.J. Swiatecki and C. F. Tsang, Ann. of Phys. **105** (1977), 427.
- 33) D.H.E. Gross and H.Kalinowski, Phys. Rep. **45** (1978), 175.
- 34) J. Knoll and R. Schaeffer, Ann. of Phys. **97** (1976), 307.